

Forecasting Periods of Strong Southward Magnetic Field Following Interplanetary Shocks

T. M. Salman^{1*}, N. Lugaz¹, C. J. Farrugia¹, R. M. Winslow¹, A. B. Galvin¹, and N. A. Schwadron¹

¹Space Science Center and Department of Physics, University of New Hampshire, Durham, NH, USA.

Key Points:

- Establish a probabilistic ensemble forecast for strong southward B_z using fast-forward shocks, solar wind, and IMF parameters in the previous 24 hours.
- Quantify the best combination of parameters to identify past analogues: B , B_z and N_p with most weight on the 30 minutes interval around the shock arrival.
- Gives on average a 14-hour warning, has a skill score of 0.64 on average, and is an improvement over any forecast with set probability.

arXiv:1812.05423v1 [physics.space-ph] 13 Dec 2018

*Department of Physics and Space Science Center, University of New Hampshire, Morse Hall, 8 College Rd, Durham, NH 03824, USA.

Corresponding author: T. M. Salman, ts1090@wildcats.unh.edu

Abstract

Long periods of strong southward magnetic fields are known to be the primary cause of intense geomagnetic storms. The majority of such events are caused by the passage over Earth of a magnetic ejecta. Irrespective of the interplanetary cause, fast-forward shocks often precede such strong southward B_z periods. Here, we first look at all long periods of strong southward magnetic fields as well as fast-forward shocks measured by the *Wind* spacecraft in a 22.4-year span. We find that 76% of strong southward B_z periods are preceded within 48 hours by at least a fast-forward shock but only about 23% of all shocks are followed within 48 hours by strong southward B_z periods. Then, we devise a threshold-based probabilistic forecasting method based on the shock properties and the pre-shock near-Earth solar wind plasma and interplanetary magnetic field characteristics adopting a “superposed epoch analysis”-like approach. Our analysis shows that the solar wind conditions in the 30 minutes interval around the arrival of fast-forward shocks have a significant contribution to the prediction of long-duration southward B_z periods. This probabilistic model may provide on average a 14-hour warning time for an intense and long-duration southward B_z period. Evaluating the forecast capability of the model through a statistical and skill score-based approach reveals that it outperforms a coin-flipping forecast. By using the information provided by the arrival of a fast-forward shock at L1, this model represents a marked improvement over similar forecasting methods. We outline a number of future potential improvements.

1 Introduction

Strong interaction of the solar wind with Earth’s magnetosphere can give rise to geomagnetic storms. *Fairfield and Cahill* [1966] identified the southward component of the interplanetary magnetic field (IMF) to be associated with ground magnetic disturbances on Earth. *Echer et al.* [2008] studied 90 intense geomagnetic storms (when the disturbed storm time index, Dst reached below -100 nT) during solar cycle 23 (1996-2006) and found all of them to be associated with strong southward B_z . Southward B_z opens the subsolar magnetopause through magnetic reconnection which allows the transfer of energy, plasma, and momentum to the magnetosphere [*Dungey*, 1961]. A criterion for intense geomagnetic storms is the presence of a long period (>3h) of large, and negative (<-10 nT) IMF B_z [*Gonzalez and Tsurutani*, 1987]. While not infallible (see e.g., *Farrugia et al.* [1998]), this is generally a very useful criterion.

The driver of such storms may be a coronal mass ejection (CME), the sheath of shocked plasma upstream of a CME, corotating interaction regions (CIRs), or a combination of these structures [*Zhang et al.*, 2007; *Kilpua et al.*, 2017]. CMEs are associated with large amounts of material ejected from the solar atmosphere into the solar wind. In particular, CMEs, and their subset magnetic clouds (MCs) are amongst the drivers of the strongest geomagnetic storms. Magnetic clouds are regions of enhanced magnetic field strength, smooth rotation of the magnetic field vector, and low proton temperature [*Burlaga et al.*, 1981]. The reasons why CMEs drive the strongest geomagnetic storms are: the southward component of magnetic field in CMEs is non-fluctuating, can be especially strong [*Huttunen et al.*, 2005; *Zhang et al.*, 2007], and can last for several hours [*Farrugia et al.*, 1997]. *Zhang et al.* [2007] investigated 88 intense geomagnetic storms (Dst \leq -100 nT) that occurred during 1996-2005 and found the majority of them (87%) to be caused by either single CMEs or multiple CMEs. *Ontiveros and Gonzalez-Esparza* [2010] studied 47 geomagnetic storms during the ascending phase of solar cycle 23 and found all of them to be associated with the passage of a shock followed by a CME. The orientation of IMF B_z along with the impulsive energy at the CME front (or CME shock) determines the severity of space weather or intensity of geomagnetic storms [*Balan et al.*, 2014].

On the other hand, CIRs are consequences of spatial variability in the coronal expansion and solar rotation, which radially aligns solar wind flows of different speeds [*Gosling and Pizzo*, 1999]. CIRs correspond to weak or moderate storms due to their fluctuating mag-

netic and velocity fields in the overtaking high-speed stream, consistent with Alfvénic waves [Tsurutani, 1995]. Either the CIR or the high-speed stream or both can be drivers of storms [Borovsky and Denton, 2006].

Apart from the structures described above, shocks or sheaths can also be geoeffective [Huttunen *et al.*, 2002]. Shocks can accelerate solar energetic particles [Reames, 1999] and the sheath regions downstream of the shocks containing IMF compressed by the shock can also drive intense geomagnetic storms [Tsurutani *et al.*, 1988]. CME sheaths are responsible for a quarter [Richardson *et al.*, 2001] to a half [Tsurutani *et al.*, 1988] of all geomagnetic storms. Lugaz *et al.* [2016] highlighted multiple ways for a shock-sheath structure to be geoeffective.

Intense geomagnetic storms are often preceded by storm sudden commencements (SSCs). SSCs serve as an indicator of the first impact of a travelling disturbance associated with a strong dynamic pressure change on the magnetosphere [Joselyn and Tsurutani, 1990]. The disturbance compresses the magnetosphere resulting in an abrupt increase of the Dst [Ontiveros and Gonzalez-Esparza, 2010]. What causes SSCs is mainly the shock waves driven by fast CMEs [Russell *et al.*, 1974; Echer and Gonzalez, 2004; Echer *et al.*, 2008]. CIR-driven storms generally lack sudden commencements [Kamide, 1998].

Strong shocks are usually found ahead of fast CMEs [Borovsky and Denton, 2006]. Thereby most SSCs are associated with strong interplanetary shocks [Iucci *et al.*, 1988; Russell *et al.*, 1992]. Gold [1955] initially suggested the association of SSCs with interplanetary shocks, which was validated by later studies. Chao and Lepping [1974] showed that out of 48 SSCs where interplanetary data are available at solar maximum between 1968 and 1971, 41 were associated with shock events. In a similar study, Smith *et al.* [1986] found nearly a one-to-one correspondence between SSCs and interplanetary shocks over solar maximum between 1978 and 1981. Gosling *et al.* [1991] found all but one of the 37 largest geomagnetic storms in the period of 1978 to 1982 to be associated with the passage of a CME and/or shock disturbances at Earth and the large majority of them (27 out of 37) to be associated with interplanetary events where Earth encountered both a shock and the CME driving it. However, CMEs/shocks are not a sufficient cause behind intense geomagnetic storms because it has also been shown that half of all CMEs and half of all shock disturbances encountered by Earth in this span did not produce any substantial geomagnetic activity.

Due to the existence of a strong correlation between southward B_z periods and geomagnetic storms, reliable prediction of B_z can be thought of as a primary basis for accurate space weather forecasting. Several studies have been carried out to predict B_z from purely statistical approaches to physics-based models and all manner of hybrids in between based on coronal data or near-Earth solar wind observations or using observations of B_z in conjunction with other solar wind parameters to form so-called “coupling functions”. However, as the IMF frequently fluctuates, predicting southward B_z is full of uncertainties [Jurac *et al.*, 2002]. Chen *et al.* [1997] argued that for particularly well-defined magnetic structures, B_z could be predicted up to approximately 10 hours in advance. These structures such as magnetic clouds have a smooth rotation of the IMF observed at L1. This allows for the extrapolation of B_z to later times when the event reaches Earth, but such a forecasting scheme has not been tested in a quantitative way yet. Kim *et al.* [2014] demonstrated a two-step forecasting technique to improve the forecast capability for geomagnetic storms. Their specific framework is based on estimating initial CME parameters and updating the forecast through monitoring of near real-time solar wind conditions. It sets out an interesting framework for considering how to best approach event-based prediction and uses a combination of parameters and approaches to address shortcomings of each other. Savani *et al.* [2015] used a combination of remote sensing and empirical relationships for predicting magnetic vectors of magnetic clouds when they reach Earth. This approach builds on the classification scheme of Bothmer and Schwenn [1998], which itself uses the helicity rule of Rust and Kumar [1994]. Related but different techniques have been proposed by Palmerio *et al.* [2017]; Moestl *et al.* [2018], which rely purely on solar and coronal observations to determine the initial “state”

of the CME. However, these techniques may not be always successful in forecasting complex geomagnetic storms (for example due to multiple CMEs) and need to be further tested over a large number of events. *Balan et al.* [2017] suggested a scheme for forecasting severe space weather based on the sudden increase in solar wind velocity due to a high-velocity CME front (or CME shock) coinciding with large southward B_z . This forecasting scheme provides a forecast time of less than 35 minutes. *Riley et al.* [2017] outlined a pattern recognition (PR) technique for forecasting B_z . Using a mean square error method, they found that the PR technique shows only limited improvement over the baseline model ($B_z=0$ always) for the prediction of B_z . They also observed that the prediction correlation generally increases for a small forecasting window of 6 hours. *Owens et al.* [2017] demonstrated an analogue ensemble (AnEn) method for probabilistic forecasting of B_z . They used a cost/loss method for determining the effectiveness of a probabilistic forecast. They found that AnEn method for probabilistic forecasting of B_z has value only for relatively small forecast lead times (3 hours) and for large negative values of B_z (<-2.93 nT).

Jurac et al. [2002] examined the influence of shock parameters on geomagnetic disturbances within 48 hours following the shock arrival at Earth. They studied 107 fast-forward shocks observed by the *Wind* spacecraft from 1995 to 2000. They identified the angle between the shock normal and the upstream IMF, θ_u to be a good indicator of future geoeffectiveness of a shock. They found that shocks with θ_u between $70-90^\circ$ are followed by intense storms 38–50% of the time. They found an even better correlation using the angle between shock normal and the downstream IMF, θ_d . They found that shocks with front normals orthogonal to the downstream IMF ($\theta_d > 80^\circ$, i.e., perpendicular shocks) are likely to be followed by intense storms 40% of the time. This study highlighted the potential for some fast-forward shocks to provide an “advanced warning” of an incoming strong southward B_z period depending on the shock parameters. To the best of our knowledge, this study has not been followed up to include more shocks and it is not currently used for real-time space weather forecasting.

In this paper, we forecast strong southward B_z periods that are preceded by fast-forward shocks. To do so, we construct a forecasting model by considering an ensemble of past analogues, similar to the procedure of *Owens et al.* [2017]. This builds upon the assumption that past variability can serve as an indicator of future variability [*Riley et al.*, 2017]. Our initial hypothesis is that the majority of strong southward B_z periods are caused by CMEs, as found by previous studies, and we decide to build our ensemble of analogues only from periods around fast-forward shocks. It is known that CME speed is somewhat correlated with CME magnetic field strength [*Moestl et al.*, 2014]. Slow CMEs and minor shock disturbances are not associated with significant geomagnetic activity [*Gosling et al.*, 1991]. Thereby, fast CMEs can be expected to drive the majority of the strong southward B_z periods. Near 1 AU, CMEs are the main drivers of fast-forward shocks [*Berdichevsky et al.*, 2000]. These periods are therefore likely to be preceded by a fast-forward shock, driven by the CME. The level of geomagnetic activity stimulated by Earth passage of a shock disturbance or CME is related directly to the magnitude of the flow speed, magnetic field strength, and southward field component associated with the event [*Russell and McPherron*, 1973; *Akasofu*, 1981; *Baker et al.*, 1984]. As a result, prediction of these variable solar wind conditions in near-Earth space (i.e., at 1 AU) is important for space weather forecasting [*Owens et al.*, 2005].

The paper is organized as follows. Data and methodology of our study are described in Section 2. We present the probabilistic forecast model for two reference events in Section 3. In Section 4, we find the best method for the prediction of strong southward B_z periods. Then, we examine the probabilistic forecasts using a statistical and skill score-based approach. A brief summary and discussion are stated in Section 5.

2 Methodology

Our model uses plasma and interplanetary magnetic field measurements for the solar wind around the arrival of a fast-forward shock at L1 (see Section 2.1 for details). We use the association between fast-forward shocks and strong and long-duration southward B_z periods as the basis of our forecasting model. As such, we are only able to forecast the arrival of a long-duration (more than 3 hours) strong southward B_z ($B_z < -10$ nT) following fast-forward shocks. Section 2.2 provides a quantitative justification of limiting the model to periods following fast-forward shocks only.

At the core of our technique is to find closest past events to the event that we wish to forecast. To do so, we select the interval of 24 hours prior to the shock to 0.25 hours after the shock arrival as the training window and the interval of 0.25 hours to 48 hours after the shock arrival as the forecast window as explained in Section 2.3. For any event to be forecasted, we use the training window to determine the closest matches to the current solar wind conditions and use the observations of the post-shock intervals of these closest matches to make a probabilistic forecast for the reference event. These closest matches are found through quantifying variations of four solar wind and interplanetary magnetic field parameters in the training window using the root mean square error (RMSE) approach.

Once the closest matches are determined, we calculate how many of these reached our southward B_z threshold ($B_z < -10$ nT for three consecutive hours or more) after the shock. The proportion of these closest matches that reach the threshold over the total number of closest matches determines the probabilistic forecast (see Section 2.4 for details).

We adopt some modifications to our technique of finding closest past events. We split the training window into two intervals as described in Section 2.5. We assign different weights to the two intervals in the training window (Section 2.5.1). RMSE of the four parameters in both intervals are multiplied with weighting constants (Section 2.5.2).

In Section 2.6, we convert the probabilistic forecasts into dichotomous forecasts by imposing a threshold criterion onto them.

2.1 Data

For our study, we select the time period of more than 22 years from 01/01/1995 to 05/27/2017. We use the shock database of *Kilpua et al.* [2015], generated and maintained at the University of Helsinki which can be found at: <http://ipshocks.fi/> and the shock database of Harvard Smithsonian Center for Astrophysics which can be found at: <https://www.cfa.harvard.edu/shocks/>. Hereafter, we will refer to these two databases as IPSDB and CFASDB respectively for brevity. For all the fast-forward *Wind* shocks with the fast magnetosonic Mach number, $M_{ms} > 1$ in this span, we select the 3-day window around a shock, containing the period from 24 hours prior to the shock to 48 hours after the shock arrival at L1. To record the solar wind conditions during these windows, we use 1-minute high resolution data from the *Wind* Magnetic Field Investigation [MFI, *Lepping et al.*, 1995] instrument & 90-second resolution plasma data from the Solar Wind Experiment [SWE, *Ogilvie*, 1995] instrument. As explained below, we focus on four parameters: magnetic field magnitude (B), z-component of the magnetic field (B_z) in GSM (Geocentric Solar Magnetospheric) coordinates, solar wind proton number density (N_p), and x-component of the solar wind velocity (V_x) in GSM coordinates. Hereafter, we refer to these 3-day windows as “events”. All of our events have the same time scale with $t = 0$ hours corresponding to the shock arrival.

2.2 Examining the Proportion of Strong Southward B_z Periods Following Fast-Forward Shocks

We first examine the association between fast-forward shocks and subsequent strong and long-duration southward B_z periods to determine if the proposed approach of focusing

on periods following fast-forward shocks is appropriate. For this study only, we use hourly near-Earth OMNI data [King and Papitashvili, 2005] of GSM B_z component extracted from NASA/GSFC's OMNI data set through OMNIWeb.

All instances in the period 01/01/1995-05/27/2017 where $B_z < -10$ nT for 3 consecutive hours or more are listed. We find 129 such instances. Then we use the two shock databases to match these instances with fast-forward shocks (with $M_{ms} > 1$) observed by the *Wind* spacecraft within the pre-48h interval of an instance. However, we mainly focus on IPSDB. Using IPSDB, we find that 81 (63%) instances are preceded by at least one fast-forward shock occurring within the pre-48h interval. Then we use CFASDB to look for *Wind* shocks which are not listed in IPSDB but may be preceding the 48 negative (not preceded by any fast-forward shock occurring within the pre-48h interval) instances. We find that 6 of these negative instances are indeed preceded by a fast-forward shock not listed in IPSDB but in CFASDB. We then use both IPSDB and CFASDB to look for ACE shocks which may have preceded the 42 remaining negative instances. We find that 11 of these are preceded by a fast-forward shock observed by the ACE spacecraft at L1. In total we find that, 98 of these instances (76%) are preceded by at least one fast-forward shock occurring within the pre-48h interval. This validates the assumption that a large portion of the strong and long-duration southward B_z periods are preceded by fast-forward shocks. We also have 2 negative instances on 10/29/2013 and on 10/30/2013 which have been reported as being preceded by shocks but considerable data gaps in the pre-48h interval might have lead to a no shock observation.

We now look at the reverse association in the period 01/01/1995-05/27/2017. We treat multiple southward B_z periods within a 24-h time interval as one. If multiple southward B_z periods are preceded by the same shock, we count that shock only once. Also, there are instances where a single southward B_z period is preceded by multiple shocks. There are 490 fast-forward shocks (with $M_{ms} > 1$ and listed in the IPSDB) observed by *Wind* at L1 and we match them with 129 strong and long-duration southward B_z periods. Out of these shocks, 100 are followed by strong and long-duration southward B_z periods. Integration of the CFASDB and inclusion of ACE shocks from the IPSDB gives us 17 more such shocks (6 *Wind* shocks from CFASDB and 11 ACE shocks from IPSDB). So, out of the 507 shocks studied in this time span, 117 (regardless of spacecraft type) are followed by strong and long-duration southward B_z periods which accounts for 23% of total. This leads to the understanding that, although the large portion of the strong and long-duration southward B_z periods occur within 48 hours after the arrival of fast-forward shocks at L1, only a small portion of fast-forward shocks are actually followed by strong southward B_z periods. We combine our shocks list with the ICME list of Richardson and Cane [2010] as done in Lugaz *et al.* [2017a] and find that 86 (~74%) of these 117 shocks are CME-driven shocks. So the majority of shocks followed by southward B_z periods are driven by CME although CME-driven shocks only represent about 72% of all fast-forward shocks at 1 AU [Kilpua *et al.*, 2015].

The time interval of our study is roughly 22.4 years. The forecast model is constructed to function by monitoring 3-day windows (1 day training window and 2 days forecast window) around a fast-forward shock arrival at L1. Removing the fast-forward shock concept from the picture, the forecast model has an uphill task of distinguishing 129 strong southward B_z windows (3.2% of total) from 4088 windows. This forecasting scheme was implemented by Riley *et al.* [2017] with only moderate success to predict the southward magnetic field. In addition, testing different approaches based on the 22.4-year span of data, and the full range of solar wind plasma and IMF parameters with different weights would require a dedicated and complex data analysis study which may not improve significantly over their model. In our current approach as proposed here, we search for physics-based constraints to narrow down the total number of windows that are "candidates" as having strong southward B_z . We do so by considering those windows preceded by a fast-forward shock. Limiting ourselves to windows around fast-forward shocks enables to develop a model aimed at distinguishing the 23% positive windows out of 507 instead of 3.2% out of 4088. However, it is

achieved at the cost of not being able to predict 24% of strong southward B_z events, those not preceded by a fast-forward shock.

We also expand upon the study of *Jurac et al. [2002]* by considering the time period 1995–2017 rather than 1995–2000 and we carry out a similar examination of 507 fast-forward shocks during this period. We find 190 shocks with upstream angles between $70\text{--}90^\circ$. However, only 42 of them are followed by an intense southward B_z period within 48 hours after the shock arrival which accounts for 22% of the total. For another shock parameter, the downstream angle, we find 200 shocks with downstream angles greater than 80° and 50 of them are followed by an intense southward B_z period within 48 hours after the shock arrival which accounts for 25% of the total. Therefore, the correlation between shock angles and geoeffectiveness observed by *Jurac et al. [2002]* does not hold true for an expanded interval and increased number of shocks. The proportion we observe for shocks with angles between $70\text{--}90^\circ$ is almost identical to the proportion we found for all fast forward shocks (23% of fast-forward shocks are followed by intense storms within 48 hours after the shock arrival at L1 regardless of any parameter criteria). As our probabilistic forecast model is based on periods following fast-forward shocks, this finding leads us to consider different combinations of upstream parameters.

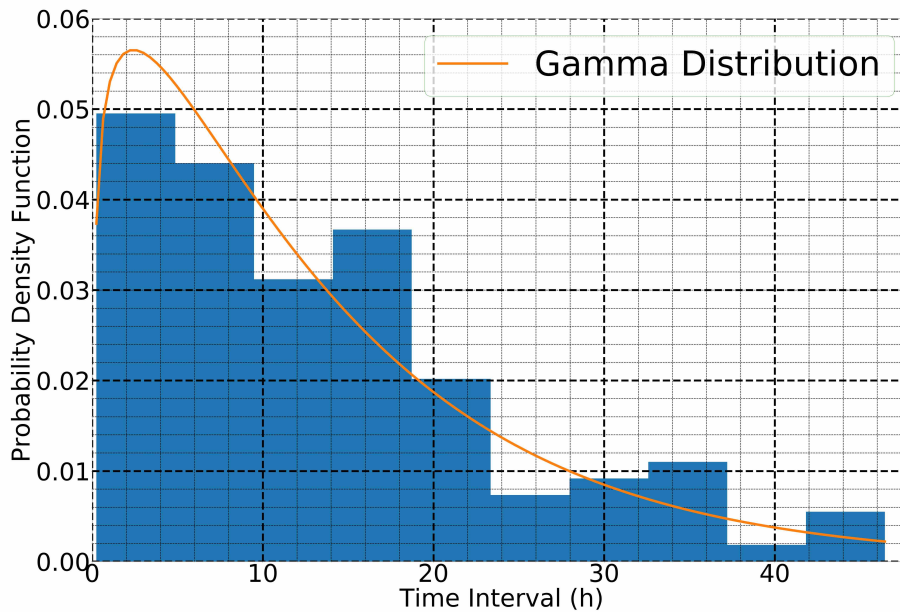


Figure 1. Distribution of time intervals between fast-forward shocks and the start time of their corresponding strong and long-duration southward B_z periods.

By examining the time intervals between fast-forward shocks and the start time of their corresponding strong and long-duration southward B_z periods, we find the mean and median of these intervals to be 13.87 hours and 11.59 hours respectively. This indicates that a forecast of strong and long-duration B_z periods based on shock arrival at L1 may give on average a 14-hour advanced warning. Examining these intervals more precisely, we observe a large range (from a minimum time interval of 15 minutes to a maximum time interval of approximately 47 hours). It is also seen that half of the time intervals lie in the range between 5.19 hours (25th percentile) and 19.15 hours (75th percentile). To first order this 25-75% range corresponds to southward B_z starting towards the back of a sheath or the beginning of

the ejecta (typical sheath duration is 7.5 hours) to the second half of the ejecta (after a 7.5-hour sheath and 11.6 hours of the ~20-hour magnetic ejecta). The shortest durations are for shocks inside CME, see *Lugaz et al.* [2015]. The greater than 75% may be at the back of a CME or in the wake or due to multiple CME interaction [*Lugaz et al.*, 2017b]. Figure 1 shows the theoretical distribution which best fits these time intervals. It is a Gamma distribution with shape parameter 1.67 and scale parameter 8.30.

2.3 Identification of Closest Matches

At the core of the forecasting technique is the idea that the shock parameters may contain information related to the driver of the shock. For example, the speed of a CME-driven shock is certainly related to the speed of the CME front. As this method is meant to be used in near-real time, it is simpler and faster not to calculate the shock speed, normal direction, etc. from the Rankine-Hugoniot relationships but instead to rely on data from the shock ramp. As such, our “training window”, where the closest matches to a reference event are identified, includes the period before the shock as well as the shock ramp itself. In details, we use the combination of the pre-shock (23.75 hours) interval and the shock itself (± 0.25 hours around the shock) as the training window and the post-shock (47.75 hours) interval as the forecast window. As we find from the time intervals that 90% of strong and long-duration southward B_z periods occur at least 1.85 hours after a shock arrival at L1, it enables us to include the post shock 0.25 hours period in the training window. For any reference event, we use the training window to determine the closest matches to the solar wind conditions to be forecasted and use observations of the corresponding post-shock intervals to make a probabilistic forecast for the reference event (see Section 2.4 for further details).

The closest matches to any reference event are found based on the variations of the four solar wind and IMF parameters of the database events in comparison with the reference event in the training window. These variations are quantified using the root mean square error (RMSE) method. We make the RMSE of a particular parameter dimensionless by dividing it by the average in the training window of that parameter of the reference event. All errors are done on dimensionless values because we do not want the RMSE of one of the parameters to dominate the calculation of TRMSE as the range of speed for example (250-1500 km/s) is very different than that of magnetic field (2-100 nT). The dimensionless RMSE for each of the four parameters (B , B_z , N_p , and V_x) are then added to get the total RMSE (TRMSE) given by:

$$TRMSE = \sum_{i=1}^4 Z_i \quad (1)$$

Z_i is the dimensionless RMSE of a parameter, i runs from 1 to 4 (four parameters in consideration).

Based on the values of TRMSE (the lower the value of TRMSE, the closer is a event to the reference), the closest matches to a reference event are identified.

2.4 Probabilistic Forecast and Error of Forecast

With the closest matches to a reference event identified, we first make a probabilistic forecast for B_z in the forecast window. Our focus is on B_z reaching a pre-defined threshold, here -10 nT for 3 consecutive hours or more in the forecast window. The probabilistic forecast goes as follows: If we focus on the N closest matches, and if M of those have B_z reaching the threshold, a probability of M/N that the reference event may have B_z reaching the threshold in its forecast window is assigned. For each probabilistic forecast, the error of the forecast is also calculated. If the reference event indeed reaches the threshold, the correct

forecast is 1 and the probabilistic error is $\sqrt{1 - (M/N)^2}$. If the reference event does not reach the threshold, the correct forecast is 0 and the probabilistic error is M/N .

The primary goal of our probabilistic forecast model is to outperform the random (i.e., coin flipping) forecast which has an error of 0.5 irrespective of whether the event reaches the threshold or not. A perfect forecasting method would have an error of 0, error of 1 means no skill. We try to minimize the error of our probabilistic forecasts. As our statistics shows that 23% of fast-forward shocks are precursors to a strong and long-duration B_z period, the best naive guess is to assign a probability of 0.23 to every fast-forward shock for causing intense southward B_z . This best zero-skill approach leads to a RMS error of 0.421. Ideally, we would like to beat this, to show that our forecast model not only has more skill than a random forecast but also possesses more skill than the best possible average-based forecast.

2.5 Modifications to the Probabilistic Forecast Model

In order to minimize the error, we randomly select 100 events from the 496 fast-forward shocks (490 listed in IPSDB + 6 additional from CFASDB) observed by *Wind* in the period 01/01/1995-05/27/2017 and remove them from the database. This way the training set is fully different from the events set and cross-contamination is negated. We then randomly slice these 100 events into four individual sets (24, 25, 25 & 26 events respectively). We use these events to form the basis of our model and refer to them as “reference events” from now on. The goal is to identify how to construct the TRMSE to minimize the error of forecasts. There is no mathematical or statistical justification for this unequal distribution of reference events. It is a mere coincidence. Among our first test set of 25 reference events, one event was removed due to a data gap issue. Then we conducted the analysis with the 24 reference events. Then expanding the results to four sets, we decided to add one more event in one of the other three sets.

2.5.1 Training Window Weighting Constant Pair (TWWCP)

The training window is split into two intervals: the first interval is the period of 24 hours to 0.25 hours prior to the shock and the second interval is the period of 0.25 hours prior to the shock to 0.25 hours after the shock arrival (it captures the shock jump). For the former interval, we bin the magnetic field and plasma data into 15-minute averages. For the latter one, the 1-minute and 90-second data is used as it is. Figure 2 shows the way the time interval is split and averaged.

For both intervals, we find the dimensionless RMSE of a parameter individually, multiply them with a weighting constant pair, and add them to get the RMSE for that particular parameter. Five sets of weighting constant pairs were tried: $(1,0)$, $(\frac{3}{4}, \frac{1}{4})$, $(\frac{1}{2}, \frac{1}{2})$, $(\frac{1}{3}, \frac{2}{3})$, and $(\frac{1}{4}, \frac{3}{4})$.

A weighting constant pair $(m, 1-m)$ means that in calculating the RMSE of a parameter in the training window, we are putting $100m\%$ weight into the variations in the -24h to -0.25h interval and $100(1-m)\%$ weight into the variations in the -0.25h to $+0.25\text{h}$ interval. Introduction of the weighting constant pair provides a key insight into the importance of both intervals to the prediction of southward B_z periods. If the probabilistic forecast improves by adding more weight into the variations of a parameter in the -0.25h to $+0.25\text{h}$ period in calculating the RMSE of that parameter in the training window, it suggests that what happens in the vicinity of the shock plays the prominent role in the occurrence of southward B_z periods after the shock arrival. If the probabilistic forecast does not improve or worsens, it suggests the pre-shock interval is the important one.

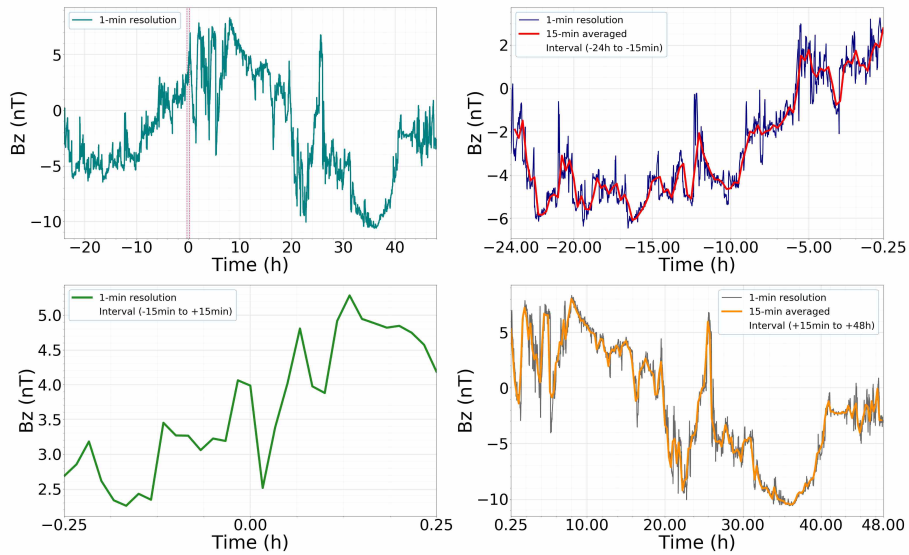


Figure 2. Wind observations of the fast-forward shock on 25 May 1997. The panels show: i) variation of GSM B_z component (top left) using 1-min resolution data over a 3-day window around the shock, from 24 May 1997 to 27 May 1997. The red dashed lines represent the interval of 0.25 hours prior to the shock arrival and 0.25 hours after the shock arrival ii) variation of GSM B_z component (top right) using 1-min resolution data and 15-min averaged data for the interval of 24 hours to 0.25 hours prior to the shock arrival iii) variation of GSM B_z component (bottom left) using 1-min resolution data for the interval of 0.25 hours prior to the shock arrival to 0.25 hours after the shock arrival iv) variation of GSM B_z component (bottom right) using 1-min resolution data and 15-min averaged data for the interval of 0.25 hours to 48 hours after the shock arrival.

2.5.2 Varying Weights of Parameter Variations

Additionally, when the TRMSE is calculated by adding the dimensionless RMSE of the four solar wind and IMF parameters, different weights are assigned to each parameter. For example, a set of weights, $a_B=1$, $a_{B_z}=1$, $a_{N_p}=0$, $a_{V_x}=0$, assigned to B, B_z , N_p , and V_x , respectively, indicates that the TRMSE in the training window is calculated with an equal weight for B and B_z , whereas the variations in N_p and V_x are neglected. These weights can have values ranging from 0 to 1 with 1 representing the maximum weight. We try out different sets of weights. In our model, the weight assigned to a particular parameter is same for both intervals of the training window. As such, the TRMSE is now given by:

$$TRMSE = \sum_{i=1}^4 a_i [mZ_{1i} + (1 - m)Z_{2i}] \quad (2)$$

Z_{1i} is the RMSE of a particular parameter in the pre-shock 23.75 hours period, Z_{2i} is the RMSE of a particular parameter in the 0.5 hours period around the shock, and a_i represents the weights assigned to the four parameters.

2.6 Threshold Forecast in Conjunction with a Criterion

In addition to the probabilistic forecasts, it can be interesting to develop dichotomous forecasts (YES/NO) that assigns a probability of 100% or 0% to an event occurring. To do so, we impose a threshold onto our probabilistic forecasts. As our model provides probabilistic forecasts based on observations in the forecast windows of 15 closest matches, we have 15 thresholds to choose from. In our analysis, we extensively tried 5, 10, and 15 closest matches. Using the 15 closest matches to identify a threshold was found to work better than using the 5 or 10 closest matches. We did not try to determine if a number of closest matches larger than 15 would be better at forecasting strong B_z period. As there are only 106 positive events in our database, many of them having different characteristics, using a larger number of closest matches is unlikely to improve the forecast much. We also found that using 10 or 15 closest matches was relatively similar. A more in-depth analysis of the most appropriate number of closest matches is left for a follow-up study.

Now, the thresholds in consideration can be generalized as $\frac{n}{15}$ where $n=1, 2, 3, \dots, 15$. Any probabilistic forecast exceeding that threshold will be considered a YES and any probabilistic forecast below that threshold will be considered a NO. Let us assume the threshold criterion selected for the probabilistic forecasts is 0.4 or $\frac{6}{15}$. So any probabilistic forecast is considered a YES if it is greater than or equal to 0.4 (number of closest matches satisfying the B_z criterion is ≥ 6) and is considered a NO if it is lower than 0.4 (number of closest matches satisfying the B_z criterion is < 6).

The skill of our threshold-based forecast model is quantified using the Heidke Skill Score (HSS, see Table 1) as reference [Heidke, 1926]. Negative skill score indicates that the model fairs worse than the random model, and positive skill score indicates the model is better than the random model. The perfect forecast will attain a HSS of 1 and a HSS of 0 means no skill.

3 Example

We demonstrate the forecasting model for a reference event observed by the *Wind* spacecraft on 18 June 2003 at 04:42 UT (Figure 3). This reference event corresponds to a shock inside a CME [Lugaz *et al.*, 2015, 2016]. Though it is not a traditional event with a shock impacting Earth first followed by a magnetic ejecta, our motivation to present this event as an example is that it illustrates the pattern of improving probabilistic forecasts better than any of the other reference events we used in our analysis. Through this event, it is possi-

Table 1. Contingency table for HSS.

Forecast	Observed		Marginal Total
	YES	NO	
YES	a (<i>Hit</i>)	b (<i>False Alarm</i>)	a+b
NO	c (<i>Miss</i>)	d (<i>Correct Negative</i>)	c+d
Marginal Total	a+c (<i>Observed YES</i>)	b+d (<i>Observed NO</i>)	a+b+c+d (<i>Total</i>)
$HSS = 2(ad-bc) / [(a+c)(c+d) + (a+b)(b+d)]$			

ble for us to showcase how including more than one parameter and putting more weight into the variations closer to the shock significantly improves the forecasts in a clear manner.

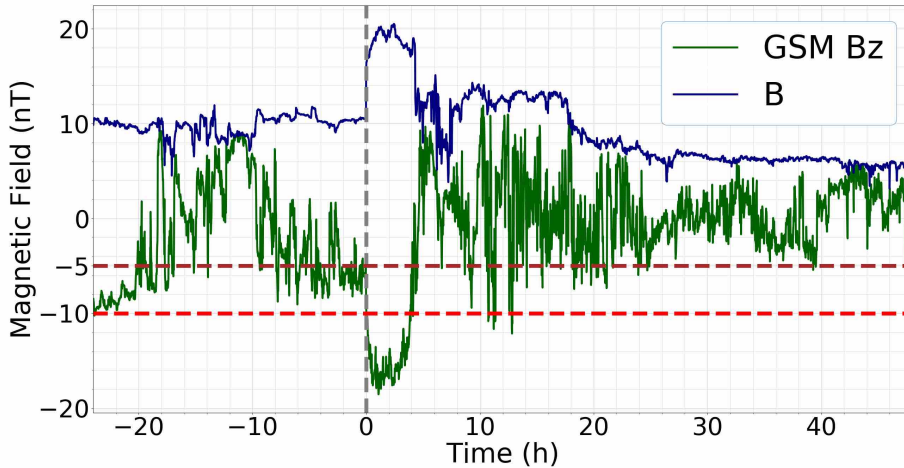


Figure 3. Wind observations of the fast-forward shock on 18 June 2003. The panel shows the variation of magnetic field strength and GSM B_z component over a 3-day window around the shock, from 17 June 2003 04:42 UT to 20 June 2003 04:42 UT.

For this reference event, the training window extends from 17 June 2003, 04:42 UT to 18 June 2003, 04:57 UT and the forecast window is the following 47.75 hours. Our goal is to predict the occurrence of at least one $B_z < -10$ nT period of 3 consecutive hours or more within the forecast window. For this reference event, 17 minutes after the shock arrival, there is the start of a period of four consecutive hours where $B_z < -10$ nT. Our expectation from the probabilistic model is to filter out the 15 closest matches to the solar wind conditions of this reference event's training window and to generate a probabilistic forecast as close as possible to 1.

Initially, we start with our baseline (only considering B_z variations and no shock info) set of weights: $B=0$, $B_z=1$, $N_p=0$, $V_x=0$ and choose (1,0) as the training window weighting constant pair (TWWCP). The TWWCP (1,0) is equivalent to (m, 1-m) of Equation 2. It means that, when we calculate the TRMSE in the training window, we put 100% weight into the variations in the -24h to -15min interval and 0% weight into the variations in the -15min to +15min interval. The weights assigned to the four parameters are summarized in

this order: $a_B, a_{B_z}, a_{N_p}, a_{V_x}$ from now on. Choice of these weights and TWWCP suggests only variations of B_z in the -24h to -15min interval prior to the shock arrival is considered. This set of weights and TWWCP gives a probabilistic forecast of 0.07 (Figure 4).

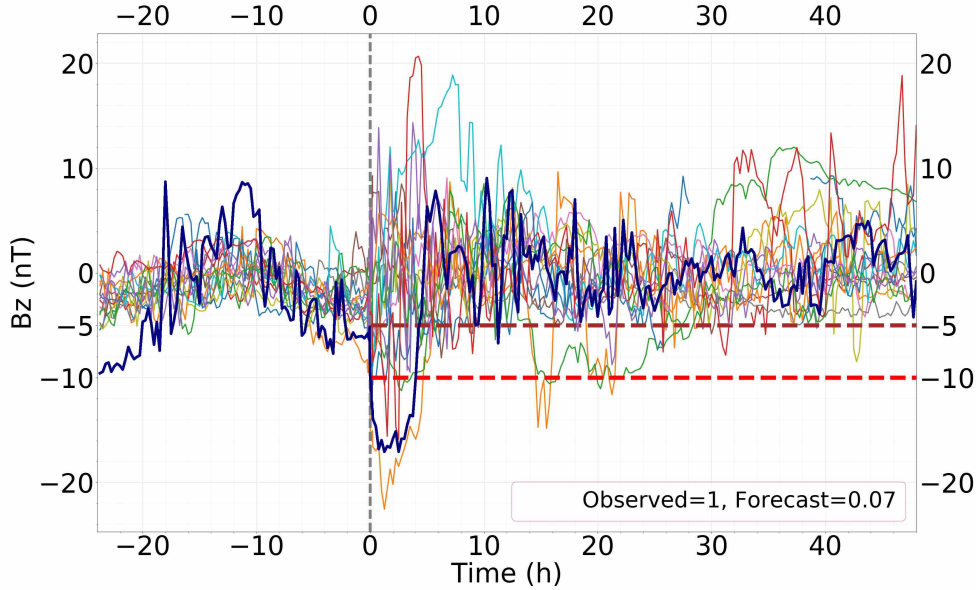


Figure 4. Probabilistic forecast for the event following the 18 June 2003 shock shown in Figure 3 for TWWCP (1,0) and weights (0, 1, 0, 0) (Navy=reference event, other colors=15 closest matches).

This probabilistic forecast is far from ideal as the prediction is a 7% probability for the occurrence of $B_z < -10$ nT periods of 3 consecutive hours or more in the forecast window compared to an observed 100% probability (as this reference event has a $B_z < -10$ nT period of 3 consecutive hours or more in its forecast window). To improve the probabilistic forecast, the TWWCP is changed from (1,0) to $(\frac{1}{2}, \frac{1}{2})$ keeping the parameter weights fixed. It gives a probabilistic forecast of 0.33. This probabilistic forecast is an improvement for sure. Next, more weight is put into the variations of B_z closer to the shock by selecting TWWCP $(\frac{1}{4}, \frac{3}{4})$ and using the same set of weights. It gives a probabilistic forecast of 0.40 (Figure 5). This improvement of the probabilistic forecast from 0.07 to 0.33 and then to 0.4 shows that putting more weight into the variations closer to the shock improves the probabilistic forecast for this particular event.

We monitor the evolution of probabilistic forecasts by changing the weights and TWWCPs. For each reference event, we accomplish this through numerous combinations of weights and TWWCPs. The goal of these repeated procedures is to identify the pattern of improving probabilistic forecasts. Thereby for this reference event, we now consider variations of both B and B_z in the training window. Use of a set of weights (0.5, 1, 0, 0) and TWWCP $(\frac{1}{4}, \frac{3}{4})$ gives a probabilistic forecast of 0.53 (Figure 6).

This improvement in the probabilistic forecast indicates considering variations of more than one parameter in finding the 15 closest matches makes the probabilistic forecast better.

This assumption is validated by a probabilistic forecast of 0.13, previously 0.07 for the set of weights (0.25, 1, 0, 0) (previously (0, 1, 0, 0)) with TWWCP (1,0) and a probabilistic forecast of 0.47, previously 0.33 for the set of weights (1, 1, 0, 0) (previously (0, 1, 0, 0))

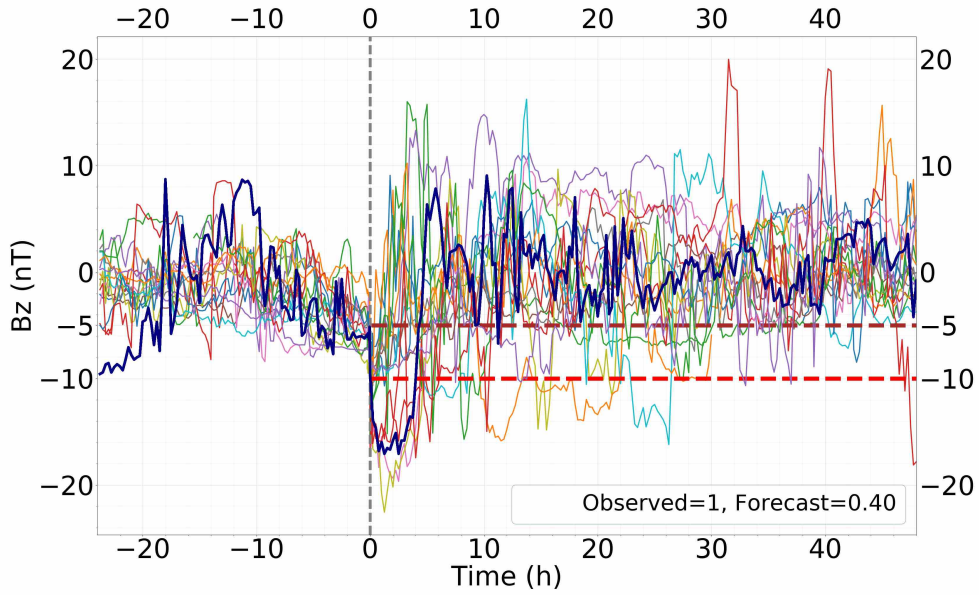


Figure 5. Same as Figure 4 but for TWWCP $(\frac{1}{4}, \frac{3}{4})$.

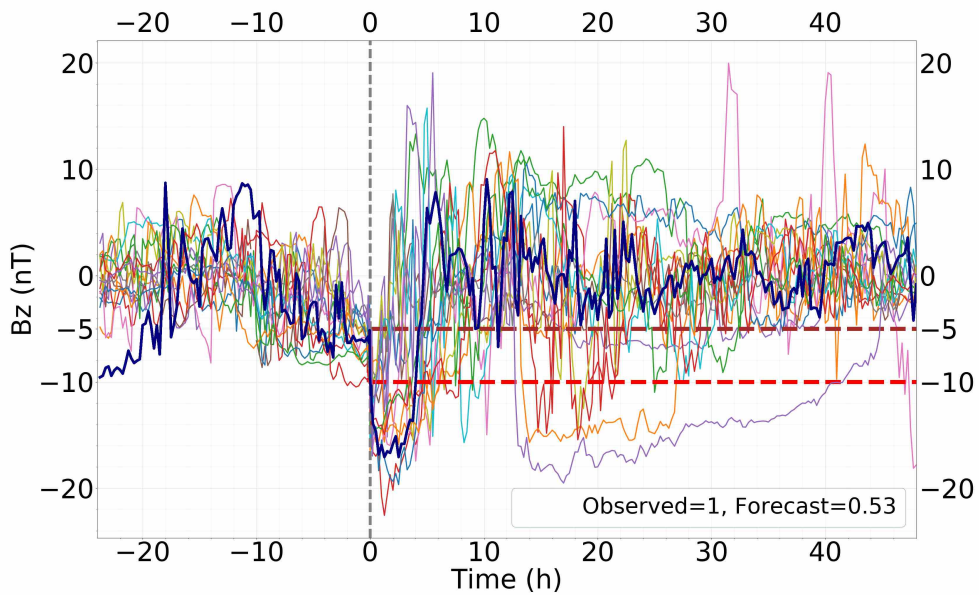


Figure 6. Same as Figure 4 but for TWWCP $(\frac{1}{4}, \frac{3}{4})$ and weights $(0.5, 1, 0, 0)$.

with TWWCP $(\frac{1}{2}, \frac{1}{2})$. We also observe improvements in the probabilistic forecasts by increasing the weight of B.

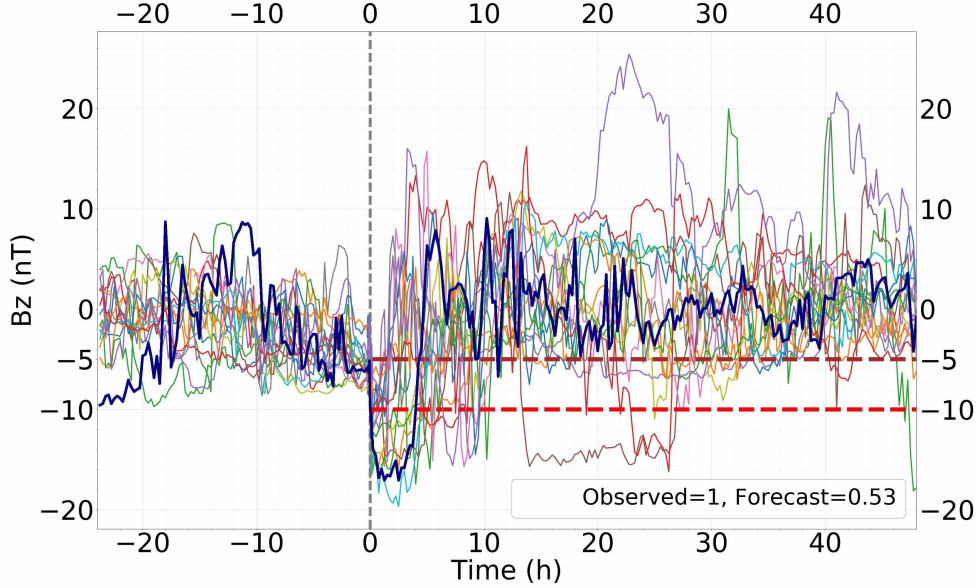


Figure 7. Same as Figure 4 but for TWWCP $(\frac{1}{4}, \frac{3}{4})$ and weights (1, 1, 0.25, 0).

After that, variations of N_p with the variations of B and B_z in the training window is considered. The set of weights (1, 1, 0.25, 0) with TWWCP $(\frac{1}{4}, \frac{3}{4})$ gives a probabilistic forecast of 0.53 (Figure 7) and the set of weights (1, 1, 0.25, 0) with TWWCP $(\frac{1}{2}, \frac{1}{2})$ gives a probabilistic forecast of 0.47. The general observed trend is that adding the parameter N_p either keeps the forecast constant or improves it.

Finally, the influence of the fourth parameter (V_x) on the probabilistic forecasts is examined. The observed trend is that adding V_x generally worsens the probabilistic forecasts. Two such scenarios are presented for a fixed TWWCP $(\frac{1}{2}, \frac{1}{2})$. The probabilistic forecast of 0.47 for the set of weights (1, 1, 0, 0) drops to 0.2 (Figure 8) for the set of weights (including V_x) (1, 1, 0, 0.5). Similarly a probabilistic forecast of 0.47 for the set of weights (1, 1, 0.25, 0) drops to 0.27 for the set of weights (including V_x) (1, 1, 0.25, 0.25). Important thing to note that this model only provides probabilistic predictions for the occurrence of strong and long-duration southward B_z periods following a fast-forward shock. The parameter V_x may have influence on the prediction of K_p or Dst.

We also highlight the threshold-based forecast. As shown in Section 4, a good criterion is a probabilistic forecast of at least 0.4.

For the reference event discussed above, the set of weights (1, 1, 0.25, 0) with TWWCP $(\frac{1}{4}, \frac{3}{4})$ gives a probabilistic forecast of 0.53. So, for the threshold criterion of 0.40, this probabilistic forecast is considered a YES and it correctly predicts the occurrence of $B_z < -10$ nT periods of 3 consecutive hours or more in the forecast window. Similarly, the set of weights (1, 1, 0, 0.5) with TWWCP $(\frac{1}{2}, \frac{1}{2})$ gives a probabilistic forecast of 0.20. So for the threshold criterion of 0.40, this forecast is considered a NO and the outcome is a missed prediction.

Figure 9 represents a second reference event for which the model is demonstrated. This event was observed by the *Wind* spacecraft on 29 March 2011 at 15:09 UT. This reference

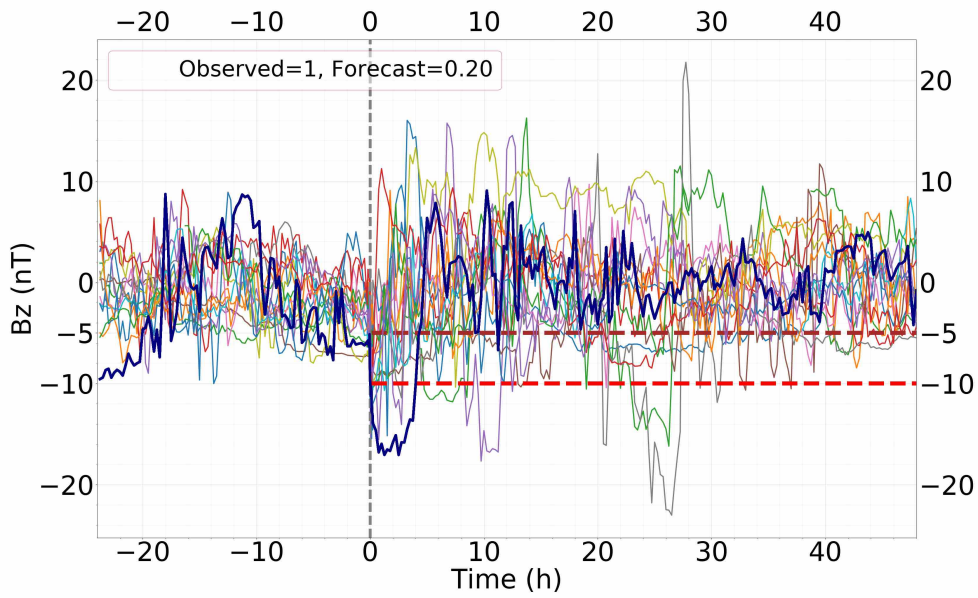


Figure 8. Same as Figure 4 but for TWWCP $(\frac{1}{2}, \frac{1}{2})$ and weights (1, 1, 0, 0.5).

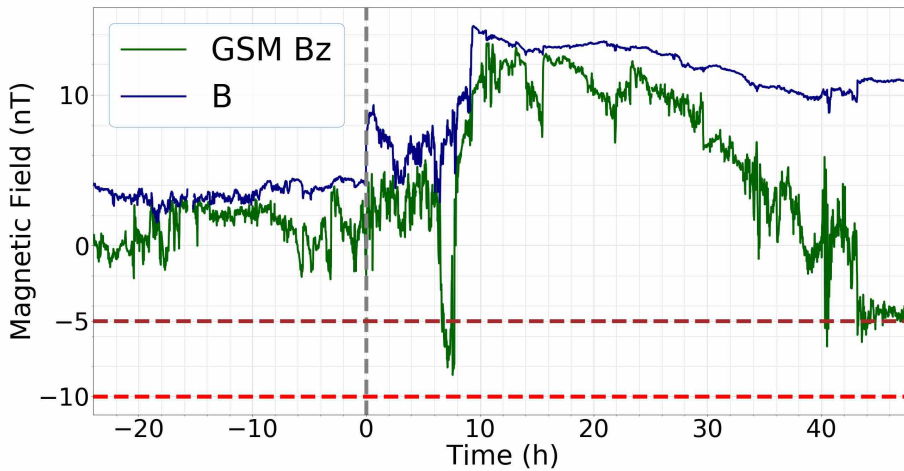


Figure 9. Wind observations of the fast-forward shock on 29 March 2011. The panel shows the variation of magnetic field strength and GSM B_z component over a 3-day window around the shock, from 28 March 2011 15:09 UT to 31 March 2011 15:09 UT.

event lies in the opposite side of the spectrum compared to the first reference event as there is no $B_z < -10$ nT period of 3 consecutive hours or more in the forecast window. Thereby, the ideal probabilistic forecast needs to be as close to 0 as possible.

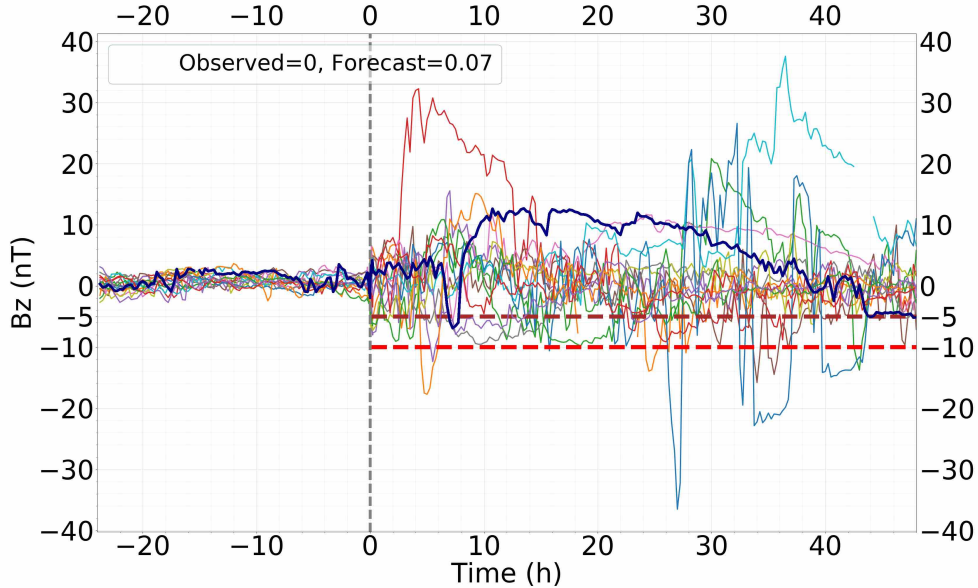


Figure 10. Probabilistic forecast for the event following the 29 March 2011 shock shown in Figure 9 for TWWCP (1,0) and weights (0, 1, 0, 0).

For the baseline set of weights (0, 1, 0, 0) and TWWCP (1,0), a probabilistic forecast of 0.07 (Figure 10) is obtained. This probabilistic forecast is almost the ideal forecast. However, recognizing the pattern of optimum probabilistic forecast is the primary goal. The trend observed from the first reference event is that adding more parameters and putting more weight into the variations closer to the shock generally improves the probabilistic forecast. However, the probabilistic forecast worsens when the variations of V_x in the training window is considered. These assumptions developed from the analysis of the first reference event are put to test here. For the set of weights (1, 0.25, 0, 0) (Figure 11) with TWWCP (1,0) a probabilistic forecast of 0.07 is obtained. The probabilistic forecast is not improved by adding a new parameter (B) like the first reference event but is not worsened either.

Next, the third parameter N_p is added and more weight is put into the variations closer to the shock. For the set of weights (1, 1, 0.5, 0) with TWWCP $(\frac{1}{3}, \frac{2}{3})$ and (1, 1, 0.5, 0) with TWWCP $(\frac{1}{4}, \frac{3}{4})$ (Figure 12), probabilistic forecasts of 0.07 is obtained for both the cases.

However, for the set of weights (1, 1, 1, 1) with TWWCP $(\frac{1}{2}, \frac{1}{2})$ probabilistic forecast of 0.20 is obtained. Similarly for the set of weights including V_x like (1, 0.5, 0.25, 0.25), (1, 1, 0, 0.5), and (0, 1, 0.25, 0.25) with fixed TWWCP $(\frac{1}{2}, \frac{1}{2})$, probabilistic forecasts of 0.20, 0.13, and 0.13 are obtained respectively which confirms the assumption that adding the parameter V_x generally makes the forecast worse. Now, for the same selected threshold of 0.40 as the first reference event, all of the predictions discussed above for the second reference event are considered a NO and the outcome is the correct prediction.

The pattern observed through the analysis of reference events (only 2 shown in this section) holds true for both positive ($B_z < -10$ nT periods of 3 consecutive hours or more in forecast window) and negative (no $B_z < -10$ nT period of 3 consecutive hours or more in

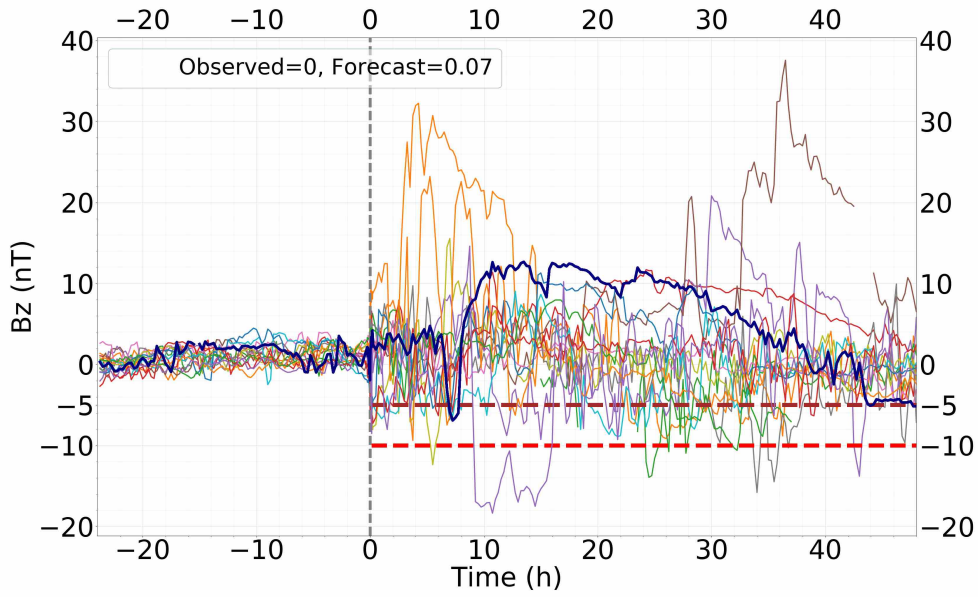


Figure 11. Same as Figure 10 but for weights (1 , 0.25, 0, 0).

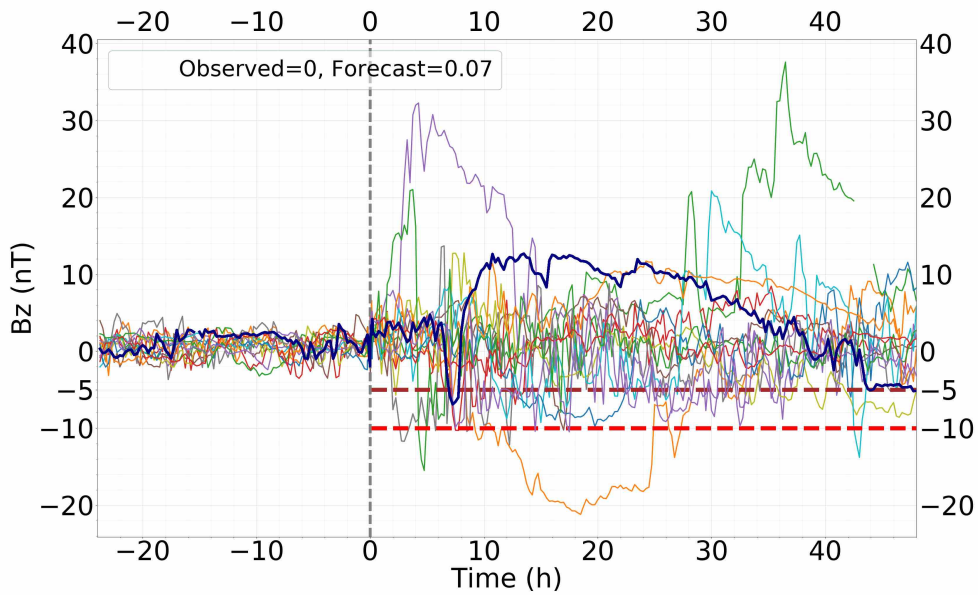


Figure 12. Same as Figure 10 but for TWWCP ($\frac{1}{4}, \frac{3}{4}$) and weights (1, 1, 0.5, 0).

forecast window) events. The probable best combination corresponds to maximum weights assigned to parameters B and B_z , inclusion of parameter N_p with reduced weight in comparison with B and B_z , exclusion of parameter V_x in identifying the closest matches, and increased weight in the 30 minutes interval around the arrival of fast-forward shocks.

4 Results

Based on the construction of our probabilistic forecast model and selection of sets of weights and TWWCPs, several thousands of different combinations can be used to build the probabilistic forecast model. However, the main goal of this study is to show that such a probabilistic and threshold-based forecast model has skills and lay the groundwork for more detailed experimentation in the future.

4.1 Best Probabilistic Forecast for All 100 Reference Events

We try out different combinations of sets of weights and TWWCPs for the first set of 24 reference events in a way similar to what is shown for the two events in Section 3. We then determine the probabilistic forecast for the forecast parameter ($B_z < -10$ nT for a period of 3 consecutive hours or more). The error of each probabilistic forecast for each reference event is calculated, as well as the RMS errors. This allows us to select the seven best performing combinations as well as the baseline forecast based only on B_z and no shock info (Table 2).

Table 2. Seven best performing and the baseline combinations of sets of weights and TWWCPs for the first set of reference events and their corresponding RMS errors of probabilistic forecasts.

Set of Weights					
B	B_z	N_p	V_x	TWWCP	RMSE (Set-I)
0	1	0	0	1,0	0.387
1	0.5	0	0	1/4,3/4	0.318
1	0.5	0.25	0	1/4,3/4	0.310
1	0.5	0.5	0	1/3,2/3	0.311
1	0.5	0.5	0	1/4,3/4	0.309
1	1	0	0	1/3,2/3	0.303
1	1	0.25	0	1/4,3/4	0.289
1	1	0.5	0	1/4,3/4	0.310

Looking at this list of 8 combinations, it is observed that the highest RMSE of 0.387 belongs to the baseline set of weights (0, 1, 0, 0) with TWWCP (1,0) and the lowest RMSE of 0.289 belongs to the set of weights (1, 1, 0.25, 0) with TWWCP ($\frac{1}{4}, \frac{3}{4}$). An important thing to note is that RMS errors for these eight combinations are well below 0.5 which means each of them is able to provide a probabilistic forecast substantially better than a random forecast. The best non-skilled forecast can be obtained by assigning a probability of 0.23 to all fast-forward shock events resulting in a RMSE of 0.421. The baseline combination has a RMSE which is 8.08% lower than this, whereas the best RMSE is significantly lower (by 31%).

Then, for each of these eight combinations, we calculate the errors of forecasts (Table 3) for the other three sets of reference events (25, 25, and 26 reference events respectively).

Table 3. Seven best performing and the baseline combinations of sets of weights and TWWCPs for the other three sets of reference events and their corresponding RMS errors of probabilistic forecasts.

Set of Weights					RMSE		
B	B_z	N_p	V_x	TWWCP	Set-II	Set-III	Set-IV
1	0.5	0	0	1/4,3/4	0.3161	0.3773	0.4716
1	0.5	0.25	0	1/4,3/4	0.3331	0.3795	0.4420
1	0.5	0.5	0	1/3,2/3	0.3564	0.3564	0.4369
1	0.5	0.5	0	1/4,3/4	0.3403	0.3612	0.4287
0	1	0	0	1,0	0.3814	0.3268	0.4427
1	1	0	0	1/3,2/3	0.3128	0.3588	0.4618
1	1	0.25	0	1/4,3/4	0.3435	0.3838	0.4551
1	1	0.5	0	1/4,3/4	0.3356	0.3915	0.4629

Finally, we calculate the average RMSE for each of these 8 combinations for all the 100 reference events (Table 4). Then we pick out 5 combinations from these 8 combinations, 4 in terms of lowest average RMS errors and the fifth one is the baseline combination. The lowest average RMSE belongs to the set of weights (1, 1, 0, 0) with TWWCP $(\frac{1}{3}, \frac{2}{3})$ which has an average RMSE of 0.3592.

Table 4. Average RMS errors of probabilistic forecasts corresponding to the seven best performing and the baseline combinations of sets of weights and TWWCPs for the four sets of reference events.

Set of Weights					Average RMSE
B	B_z	N_p	V_x	TWWCP	Average RMSE
1	0.5	0	0	1/4,3/4	0.3708
1	0.5	0.25	0	1/4,3/4	0.3662
1	0.5	0.5	0	1/3,2/3	0.3652
1	0.5	0.5	0	1/4,3/4	0.3597
0	1	0	0	1,0	0.3845
1	1	0	0	1/3,2/3	0.3592
1	1	0.25	0	1/4,3/4	0.3678
1	1	0.5	0	1/4,3/4	0.3750

4.2 Threshold-Based Probabilistic Forecast

Then we move on to the second step of the probabilistic model. For each of these 5 combinations, we try to find the best threshold criterion out of 15 (see Section 2.6) corresponding to the optimum Heidke Skill Score (HSS). To find the optimum HSS, we consider the probabilistic forecasts of the 100 reference events. Looking at the scores (Table 5), we see that the lowest best HSS of 0.31 belongs to the baseline combination for a threshold of 0.33 or $\frac{5}{15}$. The highest best HSS of 0.44 belongs to the set of weights (1, 1, 0, 0) with TWWCP ($\frac{1}{3}, \frac{2}{3}$) for a threshold of 0.40 or $\frac{6}{15}$. This HSS represents a 42% improvement over the baseline HSS.

Table 5. Threshold criterion corresponding to the optimum Heidke Skill Score for the four best performing and the baseline sets of weights and TWWCPs.

Set of Weights					$B_z < -10$ nT	
B	B_z	N_p	V_x	TWWCP	Best HSS	Threshold Criterion
0	1	0	0	1,0	0.31	0.33
1	1	0	0	1/3,2/3	0.44	0.40
1	0.5	0.25	0	1/4,3/4	0.42	0.40
1	0.5	0.5	0	1/4,3/4	0.39	0.33
1	0.5	0.5	0	1/3,2/3	0.34	0.33

Now, we use this threshold of 0.40 and the set of weights (1, 1, 0, 0) with TWWCP ($\frac{1}{3}, \frac{2}{3}$) to find the HSS for 10 randomly chosen sets, each with 166 reference events (166 events account for slightly more than $\frac{1}{3}$ of our database (Table 6). In this phase, only one forecast is generated at a time by removing only the event in consideration from the database.

Table 6. Average contingency table and HSS for 10 randomly chosen sets of 166 reference events each.

Forecast	Observed		Marginal Total
	YES	NO	
Average set			
YES	18 (<i>Hit</i>)	4 (<i>False Alarm</i>)	22
NO	12 (<i>Miss</i>)	132 (<i>Correct Negative</i>)	144
Marginal Total	30 (<i>Observed YES</i>)	136 (<i>Observed NO</i>)	166 (<i>Total</i>)
HSS	0.64		

If we examine these 10 sets, each with 166 threshold-based forecasts (Table 6), the best combination provides on average 22 YES forecasts, 18 of them are correct predictions and 4 are false alarms (average False Alarm Ratio of 0.18 indicating that on average in $\frac{2}{11}$ of the forecast for B_z periods, strong and long-duration B_z were not observed). Average Threat Score or Critical Success Index is 0.53 indicating that on average slightly greater than $\frac{1}{2}$ of strong and long-duration B_z periods (observed and/or predicted) were correctly forecast. However, the model correctly predicts on average 18 out of 30 events that occurred (average Probability of Detection Yes is 0.60 indicating that on average 60% of the observed B_z periods were correctly predicted). The average Bias (Frequency) score is 0.73 indicating strong

under-forecasting of strong and long-duration B_z periods. It is evident as the model provides on average 144 NO forecasts compared to 22 YES forecasts.

5 Discussion, Conclusions and Future Work

We developed a two step threshold-based probabilistic model for forecasting $B_z < -10$ nT periods of 3 consecutive hours or more in the 48 hours after a fast-forward shock arrival at L1. In the first step, the model provides a probabilistic forecast based on an analogue ensemble approach. A pre-defined threshold is imposed on the forecast in the second step. Any forecast exceeding this threshold is considered a YES and any forecast below this threshold is considered a NO. The forecast capability of the model is evaluated using a skill score approach.

To construct the model, we use the association between fast-forward shocks and strong and long-duration southward B_z periods as the basis. We select the interval of 24 hours prior to the shock to 0.25 hours after the shock arrival as the training window and the interval of 0.25 hours to 48 hours after the shock arrival as the forecast window. For any reference event, we use the training window to determine the closest matches to the solar wind conditions to be forecasted and use the observations of the post-shock intervals of these closest matches to make a probabilistic forecast for the reference event. These closest matches are found through quantifying variations of four solar wind and interplanetary magnetic field parameters (B , B_z , N_p , V_x) in the training window using the RMSE approach. We split the training window into two intervals (24 hours to 0.25 hours prior to the shock and 0.25 hours prior to the shock to 0.25 hours after the shock arrival). For the former interval, we bin the magnetic field and plasma data into 15-minute averages. RMS errors of the four parameters in both intervals are multiplied with weighting constants. We also assign different weights to the four parameters. We try out different combinations of sets of weights and training window weighting constant pairs for a set of reference events and determine the RMSE of forecast for each combination. Analyzing these errors for 100 reference events, we select 5 combinations (4 in terms of lowest average RMS errors and 1 as baseline). Finally, for each of these 5 combinations the threshold criterion corresponding to the optimum Heidke Skill Score (HSS) is identified. The best HSS of 0.44 for a threshold criterion of 0.40 belongs to the set of weights (1, 1, 0, 0) with TWWCP ($\frac{1}{3}$, $\frac{2}{3}$).

Examining the forecasts provided by this combination for 1660 random events, we see an average Critical Success Index of 0.53 indicating that on average slightly greater than $\frac{1}{2}$ of strong and long-duration B_z periods (observed and/or predicted) were correctly forecast.

Riley *et al.* [2017] outlined a pattern recognition technique for forecasting solar wind parameters. Forecast of any solar wind parameter into the future is made based on an ensemble of prior observations and extrapolation of information provided by these observations to make a probabilistic prediction of current time. Our baseline combination of weights (0, 1, 0, 0) with TWWCP (1,0) is closely related to the method adopted by them to forecast B_z . This particular combination shows capability for predicting B_z periods subject to certain criteria. In our limited study, this has proven to be one of the best methods for forecasting $B_z < -5$ nT periods of 1h.

However, this method does not perform well for long-duration and intense southward B_z periods, as was the focus here. The modifications applied to our threshold-based probabilistic model picks out the combination (1, 1, 0, 0) with TWWCP ($\frac{1}{3}$, $\frac{2}{3}$) and the threshold criterion 0.40 as the best method for forecasting $B_z < -10$ nT periods of 3 consecutive hours or more in the 48 hours after a fast-forward shock arrival at L1. The average RMSE associated with this combination is 0.3592 (for 100 reference events), which is 14.7% lower than the RMSE of 0.421 of the non-skilled forecast. The non-skilled forecast refers to assigning a 0.23 probability to any fast-forward shock being followed by an intense storm within 48

hours after its arrival. Quantitatively this combination is 28% better compared to the coin-flipping/random model (RMSE of 0.50).

The model would provide on average a 14-hour warning of an upcoming intense southward B_z period. This puts it in-between the L1/nowcast forecast (~30 minutes) and those based on solar/coronal data (1-3 days). Preliminary statistics shows that the model has significant skills. The basis of the model is the association between fast-forward shocks and strong and long-duration southward B_z periods. Our study validates this close association as we find 76% of strong and long-duration southward B_z periods over a 22.4-year span to be preceded by fast-forward shocks. Thereby at best we would expect the model to successfully predict 76% southward B_z periods. On a similar note, we can make the database more robust by including data from STEREO and ACE spacecraft (especially as SC24 is different and weaker from SC23, [McComas *et al.*, 2013]) and also shock-like discontinuities. Another foreseeable improvement would be to try out more combinations of sets of weights and training window weighting constant pairs to further minimize the error of forecasts. We only tried a handful of combinations based on the pattern of improving probabilistic forecasts developed through analyzing multiple reference events. The final logical improvement would be to develop a dynamic forecasting model. Our analysis shows that including post-shock information and putting more weight into solar wind variations closer to the shock have the tendency to significantly improve the probabilistic forecasts. Thereby this proposed dynamic model will give a probabilistic forecast 0.25 hours after a fast-forward shock arrival at L1. Then this forecast will be constantly updated up to a certain period through monitoring post-shock solar wind conditions. However, this evolving forecasting period can be a challenge to determine as our findings suggest that 10% of strong and long-duration southward B_z periods occur within 1.85 hours after the shock arrival. Thereby a proper balance needs to be established between advance warning and accuracy of forecasts.

In closing, we have developed a threshold-based probabilistic forecast model using a “superposed epoch analysis”-like approach. The limited trials to identify the best method to predict prolonged and intense southward B_z periods have shown encouraging signs. Preliminary statistics shows that the forecasts provided by the model are measurably better than a random model. However, the model has not been entirely successful in providing accurate and actionable forecasts. It is also uncertain how much improvement would be achieved through adopting the aforementioned refinements. We are planning to conduct a more extensive study in the future to evaluate and develop the model further. The ultimate goal is to devise a model that can function as a real-time forecasting tool. Given the underlying complexity of the solar wind and a forecast parameter like B_z which has limited inherent predictability, this model is definitely a step in the right direction.

Acknowledgments

The authors acknowledge use of NASA/GSFC’s Space Physics Data Facility’s OMNIWeb (or CDAWeb or ftp) service, OMNI data available at <https://omniweb.gsfc.nasa.gov/>, *Wind* data available at <https://cdaweb.sci.gsfc.nasa.gov/index.html/>, the Heliospheric shock database, generated and maintained at the University of Helsinki which can be found at: <http://ipshocks.fi/>, and shock database of Harvard Smithsonian Center for Astrophysics which can be found at: <https://www.cfa.harvard.edu/shocks/> and sincerely thank the corresponding teams for their open data policy. The research for this manuscript was supported by the following grants: NSF AGS-1435785, AGS-1433086 and AGS-1433213 and NASA NNX15AB87G, NNX15AU01G and NNX16AO04G. R.M.W. acknowledges support from NASA grant NNX15AW31G and NSF grant AGS1622352.

References

Akasofu, S. I. (1981), Energy coupling between the solar wind and the magnetosphere, *Space Science Reviews*, 28, 121.

- Baker, D. N., S. I. Akasofu, W. Baumjohann, J. W. Bieber, D. H. Fairfield, E. W. Hones, B. Mauk, R. L. McPherron, and T. E. Moore (1984), Substorms in the magnetosphere, Chapter 8, NASA Scientific and Technical Information branch, *NASA Ref. Publ.*, 1120.
- Balan, N., R. Skoug, S. Tulasi Ram, P. K. Rajesh, K. Shiokawa, Y. Otsuka, I. S. Batista, Y. Ebihara, and T. Nakamura (2014), CME front and severe space weather, *J. Geophys. Res. (Space Physics)*, 119, 10,041–10,058, doi:10.1002/2014JA020151.
- Balan, N., Y. Ebihara, R. Skoug, K. Shiokawa, I. S. Batista, S. Tulasi Ram, Y. Omura, T. Nakamura, and M. C. Fok (2017), A scheme for forecasting severe space weather, *J. Geophys. Res. (Space Physics)*, 122, 2824–2835, doi:10.1002/2016JA023853.
- Berdichevsky, D. B., A. Szabo, R. P. Lepping, A. F. Vinas, and F. Mariani (2000), Interplanetary fast shocks and associated drivers observed through the 23rd solar minimum by Wind over its first 2.5 years, *J. Geophys. Res.*, 105, 27,289–27,314, doi:10.1029/1999JA000367.
- Borovsky, J. E., and M. H. Denton (2006), Differences between CME-driven storms and CIR-driven storms, *J. Geophys. Res.*, 111, A07S08, doi:10.1029/2005JA011447.
- Bothmer, V., and R. Schwenn (1998), The structure and origin of magnetic clouds in the solar wind, *Annales Geophysicae*, 16, 1–24, doi:10.1007/s00585-997-0001-x.
- Burlaga, L., E. Sittler, F. Mariani, and R. Schwenn (1981), Magnetic loop behind an interplanetary shock - Voyager, Helios, and IMP 8 observations, *J. Geophys. Res.*, 86, 6673–6684.
- Chao, J. K., and R. P. Lepping (1974), A correlative study of sscs, interplanetary shocks, and solar activity, *J. Geophys. Res.*, 79, 1799, doi:10.1029/JA079i013p01799.
- Chen, J., P. J. Cargill, and P. J. Palmadesso (1997), Predicting solar wind structures and their geoeffectiveness, *J. Geophys. Res.*, 102, 14,701–14,720.
- Dungey, J. W. (1961), Interplanetary Magnetic Field and the Auroral Zones, *Phys. Rev. Lett.*, 6, 47, doi:10.1103/PhysRevLett.6.47.
- Echer, E., and W. D. Gonzalez (2004), Geoeffectiveness of interplanetary shocks, magnetic clouds, sector boundary crossings and their combined occurrence, *Geophys. Res. Lett.*, 31, L09,808, doi:10.1029/2003GL019199.
- Echer, E., W. D. Gonzalez, B. T. Tsurutani, and A. L. C. Gonzalez (2008), Interplanetary conditions causing intense geomagnetic storms ($Dst \leq -100$ nT) during solar cycle 23 (1996–2006), *J. Geophys. Res.*, 113, A05,221, doi:10.1029/2007JA012744.
- Fairfield, D. H., and J. L. J. Cahill (1966), Transition region magnetic field and polar magnetic disturbances, *J. Geophys. Res.*, 71, 155–169.
- Farrugia, C. J., L. F. Burlaga, and R. P. Lepping (1997), Magnetic Clouds and the quiet/storm effect at Earth: A review, in *Magnetic Storms*, edited by B. T. Tsurutani, W. D. Gonzalez, Y. Kamide, and J. K. Arballo, *Geophysical Monogr. Ser.*, 98, 91.
- Farrugia, C. J., J. D. Scudder, M. P. Freeman, L. Janoo, G. Lu, J. M. Quinn, R. Arnoldy, R. B. Torbert, L. F. Burlaga, K. W. Ogilvie, R. P. Lepping, A. J. Lazarus, J. T. Steinberg, F. T. Gratton, and G. Rostoker (1998), Geoeffectiveness of three Wind magnetic clouds: A comparative study, *J. Geophys. Res.*, 103, 17,261.
- Gold, T. (1955), Discussion on Shock Waves and Rarefied Gas Dynamics, *Gas Dynamics of Cosmic Clouds (Proceedings from IAU Symposium)*, 2, 97–105.
- Gonzalez, W. D., and B. T. Tsurutani (1987), Criteria of interplanetary parameters causing intense magnetic storms (Dst of less than -100 nT), *Planetary and Space Science*, 35, doi:10.1016/0032-0633(87)90015-8.
- Gosling, J. T., and V. J. Pizzo (1999), Formation and evolution of corotating interaction regions and their three dimensional structure, *Space Science Reviews*, 89, 21–52.
- Gosling, J. T., D. J. McComas, J. L. Phillips, and S. J. Bame (1991), Geomagnetic activity associated with Earth passage of interplanetary shock disturbances and coronal mass ejections, *J. Geophys. Res.*, 96, 7831–7839.
- Heidke, P. (1926), Berechnung des Erfolges und der Gute der Windstarkevorhersagen im Sturmwarnungsdienst, *Geografiska Annaler*, 8, 301–349, doi:10.2307/519729.
- Huttunen, K. E. J., H. E. J. Koskinen, and R. Schwenn (2002), Variability of magnetospheric

- storms driven by different solar wind perturbations, *J. Geophys. Res.*, *107*, 1121, doi:10.1029/2001JA900171.
- Huttunen, K. E. J., R. Schwenn, V. Bothmer, and H. E. J. Koskinen (2005), Properties and geoeffectiveness of magnetic clouds in the rising, maximum and early declining phases of solar cycle 23, *Ann. Geophys.*, *23*, 625, doi:10.5194/angeo-23-625-2005.
- Iucci, N., M. Parisi, M. Storini, and G. Villaresi (1988), A compilation of geomagnetic sudden commencements (SSCs): Their origin and the associated interplanetary disturbances and cosmic ray variations (1966/1974), *Astron. Astrophys. Suppl. Ser.*, *72*, 369.
- Joselyn, J. A., and B. T. Tsurutani (1990), Geomagnetic sudden impulses and storm sudden commencements: a note on terminology, *EOS Trans.*, *71*, 1808, doi:10.1029/90EO00350.
- Jurac, S., J. C. Kasper, J. D. Richardson, and A. J. Lazarus (2002), Geomagnetic disturbances and their relationship to Interplanetary shock parameters, *Geophys. Res. Lett.*, *29*(10), 1463, doi:10.1029/2001GL014034.
- Kamide, Y. (1998), Current understanding of magnetic storms: Storm-substorm relationships, *J. Geophys. Res.*, *103*, 17,705.
- Kilpua, E. K. J., E. Lumme, K. Andreeva, A. Isavnin, and H. E. J. Koskinen (2015), Properties and drivers of fast interplanetary shocks near the orbit of the Earth (1995-2013), *J. Geophys. Res. (Space Physics)*, *120*, 4112–4125, doi:10.1002/2015JA021138.
- Kilpua, E. K. J., A. Balogh, R. von Steiger, and Y. D. Liu (2017), Geoeffective Properties of Solar Transients and Stream Interaction Regions, *Space Science Reviews*, *212*, 1271–1314, doi:10.1007/s11214-017-0411-3.
- Kim, R. S., Y. J. Moon, N. Gopalswamy, Y. D. Park, and Y. H. Kim (2014), Two-step forecast of geomagnetic storm using coronal mass ejection and solar wind condition, *Space Weather*, *12*, 246–256, doi:10.1002/2014SW001033.
- King, J. H., and N. E. Papitashvili (2005), Solar wind spatial scales in and comparisons of hourly Wind and ACE plasma and magnetic field data, *J. Geophys. Res.*, *110*, A02,104.
- Lepping, R. P., M. H. Acuna, and L. F. Burlaga (1995), The WIND magnetic field investigation, *Space Science Reviews*, *71*, 207–229, doi:10.1007/BF00751330.
- Lugaz, N., C. J. Farrugia, C. L. Huang, and H. E. Spence (2015), Extreme geomagnetic disturbances due to shocks within CMEs, *Geophys. Res. Lett.*, *42*, 4694–4701, doi:10.1002/2015GL064530.
- Lugaz, N., C. J. Farrugia, R. M. Winslow, N. Al-Haddad, E. K. J. Kilpua, and P. Riley (2016), Factors affecting the geoeffectiveness of shocks and sheaths at 1 AU, *J. Geophys. Res. (Space Physics)*, *121*, doi:10.1002/2016JA023100.
- Lugaz, N., C. J. Farrugia, R. M. Winslow, C. R. Small, T. Manion, and N. P. Savani (2017a), Importance of CME Radial Expansion on the Ability of Slow CMEs to Drive Shocks, *The Astrophysical Journal*, *848*, 75, doi:10.3847/1538-4357/aa8ef9.
- Lugaz, N., M. Temmer, Y. Wang, and C. J. Farrugia (2017b), The Interaction of Successive Coronal Mass Ejections: A Review, *Solar Phys.*, *292*, 64, doi:10.1007/s11207-017-1091-6.
- McComas, D. J., N. Angold, H. A. Elliott, G. Livadiotis, N. A. Schwadron, R. M. Skoug, and C. W. Smith (2013), Weakest Solar Wind of the Space Age and the Current “Mini” Solar Maximum, *The Astrophysical Journal*, *779*, 10, doi:10.1088/0004-637X/779/1/2.
- Moestl, C., K. Amla, J. R. Hall, P. C. Liewer, E. M. De Jong, R. C. Colaninno, A. M. Veronig, T. Rollett, M. Temmer, V. Peinhart, J. A. Davies, N. Lugaz, Y. D. Liu, C. J. Farrugia, J. G. Luhmann, B. Vrsnak, R. A. Harrison, and A. B. Galvin (2014), Connecting Speeds, Directions and Arrival Times of 22 Coronal Mass Ejections from the Sun to 1 AU, *The Astrophysical Journal*, *787*(2), 119, doi:10.1088/0004-637X/787/2/119.
- Moestl, C., T. Amerstorfer, E. Palmerio, A. Isavnin, C. J. Farrugia, and C. Lowder (2018), Forward modeling of coronal mass ejection flux ropes in the inner heliosphere with 3DCORE, *Space Weather*, *16*, 216–229, doi:10.1002/2017SW001735.
- Ogilvie, K. W. (1995), SWE, a comprehensive plasma instrument for the Wind spacecraft, *Space Science Reviews*, *71*, 55–77.
- Ontiveros, V., and J. A. Gonzalez-Esparza (2010), Geomagnetic storms caused by shocks

- and ICMEs, *J. Geophys. Res.*, *115*, A10,244, doi:10.1029/2010JA015471.
- Owens, M. J., P. J. Cargill, C. Pagel, G. L. Siscoe, and N. U. Crooker (2005), Characteristic magnetic field and speed properties of interplanetary coronal mass ejections and their sheath regions, *J. Geophys. Res.*, *110*, A01,105, doi:10.1029/2004JA010814.
- Owens, M. J., P. Riley, and T. S. Horbury (2017), Probabilistic solar wind and geomagnetic forecasting using an analogue ensemble or “similar day” approach, *Solar Phys.*, *292*, 69.
- Palmerio, E., E. K. J. Kilpua, A. W. James, L. M. Green, J. Pomoell, A. Isavnin, and G. Valori (2017), Determining the Intrinsic CME Flux Rope Type Using Remote-sensing Solar Disk Observations, *Solar Phys.*
- Reames, D. V. (1999), Particle acceleration at the Sun and in the heliosphere, *Space Science Reviews*, *90*, 413–491.
- Richardson, I. G., and H. V. Cane (2010), Near-Earth Interplanetary Coronal Mass Ejections During Solar Cycle 23 (1996-2009): Catalog and Summary of Properties, *Solar Phys.*, *264*, 189–237, doi:10.1007/s11207-010-9568-6.
- Richardson, I. G., E. W. Cliver, and H. V. Cane (2001), Sources of geomagnetic storms for solar minimum and maximum conditions during 1972-2000, *Geophys. Res. Lett.*, *28*, 2569–2572, doi:10.1029/2001GL013052.
- Riley, P., M. Ben-Nun, J. A. Linker, and M. J. Owens (2017), Forecasting the properties of the solar wind using simple pattern recognition, *Space Weather*, *15*, 526–540, doi:10.1002/2016SW001589.
- Russell, C. T., and R. L. McPherron (1973), The magnetotail and substorms, *Space Science Reviews*, *15*, 205.
- Russell, C. T., R. L. McPherron, and R. K. Burton (1974), On the cause of geomagnetic storms, *J. Geophys. Res.*, *79*, 1105–1109.
- Russell, C. T., M. Ginskey, S. Petrinec, and G. Le (1992), The effect of solar wind dynamic pressure changes on low and mid-latitude magnetic records, *Geophys. Res. Lett.*, *19*, 1227.
- Rust, D. M., and A. Kumar (1994), Helical magnetic fields in filaments, *Solar Phys.*, *155*, 69–97, doi:10.1007/BF00670732.
- Savani, N. P., A. Vourlidas, A. Szabo, M. L. Mays, I. G. Richardson, B. J. Thompson, A. Pulkkinen, R. Evans, and T. Nieves-Chinchilla (2015), Predicting the magnetic vectors within coronal mass ejections arriving at Earth: 1. Initial architecture, *Space Weather*, *13*, 374–385, doi:10.1002/2015SW001171.
- Smith, E. J., J. A. Slavin, R. D. Zwickl, and S. J. Bame (1986), Shocks and storm sudden commencements, in *Solar Wind Magnetosphere Coupling, Astrophysics and Space Science Library*, *126*, 345–365.
- Tsurutani, B. T. (1995), Interplanetary origin of geomagnetic activity in the declining phase of the solar cycle, *J. Geophys. Res.*, *100*, 717–733.
- Tsurutani, B. T., W. D. Gonzalez, F. Tang, and E. J. Akasofu, S. I. Smith (1988), Origin of the interplanetary southward magnetic fields responsible for the major magnetic storms near solar maximum (1978-1979), *J. Geophys. Res.*, *93*, 8519.
- Zhang, J., I. G. Richardson, D. F. Webb, N. Gopalswamy, E. Huttunen, J. C. Kasper, N. V. Nitta, W. Poomvises, B. J. Thompson, C. C. Wu, S. Yashiro, and A. N. Zhukov (2007), Solar and interplanetary sources of major geomagnetic storms ($Dst \leq -100$ nT) during 1996-2005, *J. Geophys. Res.*, *112*, A10,102, doi:10.1029/2007JA012321.